The Astrophysical Journal, 552:133–143, 2001 May 1

OBSERVATIONS OF CO $J = 3$–2 IN THE OUTFLOW OF THE STARBURST GALAXY M82

E. R. Seaquist
Department of Astronomy, University of Toronto, St. George Campus, 60 St. George Street, Toronto, ON M5S 1A7, Canada
AND
Jason Clark
Department of Physics and Astronomy, University of Manitoba, Winnipeg, MB R3T 2N2, Canada
Received 2000 September 19; accepted 2001 January 1

ABSTRACT

Observations are presented of the distribution of ^{12}CO $J = 3$–2 emission in the starburst galaxy M82 covering a region $3'' \times 3''$ (2.8 × 2.8 kpc). This area includes the halo region involved in the superwind outflow. More limited coverage is presented for ^{13}CO $J = 3$–2 and C^{18}O $J = 3$–2. The mass of molecular gas in the halo is about 5×10^8 $M_\odot$, with a dynamical timescale of the order of 10^7 yr. The results show the region of the outflow at higher CO excitation than previous published observations. Comparison with recently made observations of ^{12}CO $J = 2$–1 shows that the CO gas becomes progressively de-excited at larger distances from the starburst disk, and the isotopic ratio ^{13}CO/^{12}CO $J = 3$–2 also becomes smaller outside the starburst disk. These effects are interpreted as differences in excitation and optical depth between the starburst region and the outflow and outer disk. A comparison between the ^{12}CO $J = 3$–2 emission with a published 850 μm continuum map shows that CO makes a significant contribution to the continuum in this band and that the fractional contribution is greatest near $\pm 30''$ from the nucleus approximately along the major axis. The progressively slower rotation of the halo gas with distance above and below the disk, coupled with consideration of the conservation of angular momentum, is analyzed to reveal the pattern of the outflow. The flow appears to diverge more strongly below the disk, with a cone angle of about 90°, which compares to about 40° above the disk. The mass and energetics of the halo molecular gas suggest the possibility that the molecular material and dust in the halo will not escape from M82 but are instead being recycled through the halo after injection as supershells by one or more transient starburst events.

Subject headings: galaxies: individual (M82) — galaxies: ISM — galaxies: nuclei — galaxies: starburst — radio lines: ISM

1. INTRODUCTION

The starburst galaxy M82 is the nearest, and hence the most well-studied, object of its class, with a distance of 3.25 Mpc (Tammann & Sandage 1968). Despite the very large amount of existing data on this object in essentially all wavebands, new observations are continually being added to the M82 database, permitting further refinements in understanding the anatomy of the starburst phenomenon. Much of the new data is in the millimeter/submillimeter region, which measures conditions in the cool molecular gas and dust in the central 500 pc star-forming ring, or starburst disk. The present paper focuses on the outflow from the starburst region, based on new observations of the $J = 3$–2 transitions ^{12}CO, ^{13}CO, and C^{18}O extending up to 1.5 kpc above and below the plane of the disk. This is the highest transition used to date to map a significant portion of the outflow originating in the starburst disk.

Observations of the outflow or halo have been made by many investigators covering many wavebands, leading to the following picture: A high supernova rate in the galaxy heats the interstellar gas, producing a strong, high-speed wind at several thousand km s^{-1} comprising gas at $\sim 10^7$ K. This rarefied wind entrains cosmic rays, warm gas, and cool gas and dust, rendering the outflow visible in essentially all wavebands. Typical outflow speeds for the entrained warm and cool components are several hundred kilometers per second. Similar outflows are observed in a number of other starburst galaxies, for example, NGC 253 and NGC 4631. A general summary of this phenomenon is given by Alton, Davies, & Bianchi (1999). The proximity of M82 makes it possible to observe the region of interaction between the star-forming regions and the halo, including expanding shells and "chimneys," which are producing a clearer picture of the driving mechanism for the outflows (Weiss et al. 1999; Wills et al. 1999). The present paper provides new comparisons among ^{12}CO $J = 3$–2, ^{13}CO $J = 3$–2, C^{18}O $J = 3$–2, and ^{12}CO $J = 2$–1. For the latter measurements, use is made of data provided by N. Neininger (2000, private communication). New insights into physical conditions and kinematics of the outflow are derived, primarily associated with the outflow. A brief comparison is also made to the 850 μm continuum observations by Alton et al. (1999).

2. OBSERVATIONS

Our observations were conducted with the James Clerk Maxwell Telescope[1] (JCMT) during a series of observing runs on 1998 April 2–3, 1999 February 24, March 2–3, October 29, November 17, and April 15. The transitions observed were ^{12}CO $J = 3$–2 (345.796 GHz), ^{13}CO $J = 3$–2 (330.588 GHz), and C^{18}O $J = 3$–2 (329.331 GHz). The receiver B3 was used with dual circular polarization, sideband rejection, and either lower or upper sideband, depending on the system temperature. The single sideband system temperatures ranged from 360 to 630 K for most of the observations, but occasional values as high as 830 K were experienced, depending on weather and source elevation.

[1] The JCMT is operated by the Joint Astronomy Centre in Hilo, Hawaii on behalf of the partner organizations PPARC in the UK, the NRC of Canada, and the Netherlands Organization for Scientific Research.

The 1024 channel Dutch Autocorrelation Spectrometer was used with a bandwidth of 920 MHz (800 km s^{-1}) and a channel spacing of 1.25 MHz (1.08 km s^{-1} at ^{12}CO). All spectra were centered at an LSR velocity of 200 km s^{-1}. The FWHM beam size of the telescope is 14″ at these frequencies. Beam switching in azimuth at a rate of 1.0 Hz was employed. The beam throw used was 120″ for the central portions of the mapped regions and 180″ for the outer regions. Telescope pointing was checked by periodically monitoring strong pointing calibrators such as Mars, Saturn, W3 OH, IRC +10216, 3C 273, or 4C 39.25. The overall rms pointing uncertainty averaged over all observing runs was found to be 2″.3 in azimuth and 2″.2 in elevation, which is a small fraction of the telescope beam size.

All observations were made by sampling on a grid aligned with the major axis at P.A. = 75° and centered on the IR nucleus at $\alpha(2000) = 09^{h}55^{m}52^{s}.3$, $\delta(2000) = 69°40'46''$ (Dietz et al. 1986). The ^{12}CO observations covered a region 196″ × 196″ (28 × 28 grid). The sampling interval was 7″ (i.e., half-beam width) for the inner 11 × 7 grid and 14″ (full-beam width) for the outer region. The integration time per point was 1 minute for each of the two circular polarizations. The ^{13}CO observations were sampled on the inner 11 × 7 grid only at 7″ spacing with integration times of 3 minutes per point, and the $C^{18}O$ observations covered only five points along the major axis, spaced at 7″, with 20 minutes of integration per point. The beam efficiency of the telescope was calibrated using Saturn and found to be consistent within 10% with the value of $\eta_{MB} = 0.63$ provided in the JCMT documentation.

3. RESULTS

The data cubes were binned over 10 spectral line channels, yielding velocity channel separations of 10.8, 11.3, and 11.4 km s^{-1} at the ^{12}CO, ^{13}CO, and $C^{18}O$ transitions, respectively. In addition, a 7″ Gaussian interpolation was used on the ^{12}CO data to fill in the missing grid points in the undersampled outer region. This is equivalent to a convolution of the 14″ map to 16″ (precise value: 15″.7). The ^{13}CO data were smoothed to the same resolution for comparison with the ^{12}CO data. The results for ^{12}CO are shown in Figures 1–6 as channel maps (Fig. 1), position-velocity (p-v) plots (Fig. 2), a map of the integrated intensity, or zeroth moment (Fig. 3), and mean velocity, or the first moment (Fig. 4). Figure 5 shows a series of "rotation curves" above and below the plane, and Figure 6 shows the mean velocities measured along the minor axis. All intensities are expressed as main-beam brightness temperatures $T_{MB} = T_A^*/\eta_{MB}$, where $\eta_{MB} = 0.63$. The channel maps are displayed at velocity intervals of 21.7 km s^{-1} (after Hanning smoothing). The p-v plots show position measured parallel to the major axis at various distances (z) from the major axis above and below the plane. The integrated intensities in Figure 3 correspond to sums from 0 to 450 km s^{-1}. The results for the isotopes are shown in Figures 7 and 8. Figure 7 shows a map of the integrated intensity from 0 to 450 km s^{-1} over part of the region covered, and Figure 8 shows the ^{13}CO and $C^{18}O$ data for the starburst disk as a series of profiles together with the profiles of the main transitions for comparison.

3.1. *Instrumental Effects*

It is important to note that although the rms pointing error appears small compared to the beam, larger excursions were also noted, up to approximately twice the rms values. Such errors are distributed somewhat randomly throughout the map and not just as a systematic shift in the positions of all map features. These errors have a small effect in most regions of the map but can cause larger distortions in the measured brightness where the gradient is large (i.e., at points offset 7″–14″ from the major axis) and on the alignment of maps of different transitions (see § 3). We also searched for spurious signals introduced by beam switching at the edges of the map in Figure 3, which show up as profiles with negative intensity. Beam switching was found to affect only the outermost rows and columns of the 14 × 14 grid, and consequently the extreme outer grid points were ignored in the analysis.

Another error affecting regions of low brightness is introduced by the error beam of the telescope, i.e., the low-level plateau extending beyond the main beam caused by random irregularities in the reflector surface. The error beam cannot be reliably deconvolved because its features vary with temperature and elevation, and with the surface adjustments made between observing periods. The error beam thus places a limit on the dynamic range of the map. The effect of the error beam on Figure 3 was assessed as follows: The distribution of integrated brightness of ^{12}CO was modeled by using a variety of double two-dimensional Gaussian models, and each model was convolved with a recent map of the telescope beam (including the error beam) measured at 850 μm. The model yielding the best match to the observed minor axis profile of M82 over the inner ±20″ was compared with the minor axis profile over the outer 40″–60″. The conclusion is that the error beam may contribute up to 30% of the observed brightness in this range above the plane and 5%–10% over the same range below the plane.

3.2. *Overview of Features of the Cube in* ^{12}CO $J = 3$–2

Figures 1, 2, and 4 show clearly the effect of rotation of the inner region of the disk, as shown in numerous previous studies at lower transitions (e.g., Sofue et al. 1992; Shen & Lo 1995). The systemic velocity derived from the rotation curve along the major axis in Figure 5 is $V_{LSR} = 210 \pm 10$ km s^{-1}, which is slightly lower (but within the errors) of the value 225 ± 10 km s^{-1}, derived by Shen & Lo (1995) from CO $J = 1$–0, and slightly higher than the figure of 200 km s^{-1}, derived by Achtermann & Lacy (1995), from the kinematics associated with the [Ne II] line emission. The value of 210 km s^{-1} occurs at a position 3″.5 (55 pc) west of our reference position (the 2 μm peak) along the major axis. The displacement is only about 1″ for a value of 225 km s^{-1}.

Figure 3 reveals a number of features associated with the outflow of molecular gas from the starburst region. The CO brightness is higher in the southern part of the outflow than in the northern. This asymmetry is evident also in both the centimeter radio and X-ray bands (see, e.g., Watson, Stanger, & Griffiths 1984; Seaquist & Odegard 1991; Reuter et al. 1994; Bregman, Schulman, & Tomisaka 1995) as well as in the optical (see, e.g., Shopbell & Bland-Hawthorn 1998). The brightness in CO is particularly high toward the southeast, where a bright feature, possibly a spur, is especially prominent. It appears to radiate outward from the vicinity of the east side of the molecular ring. There is also evidence for similar but weaker features emanating northward from the east and west sides of the ring. Similar spurlike features are seen at CO $J = 1$–0 (Nakai et al. 1987)

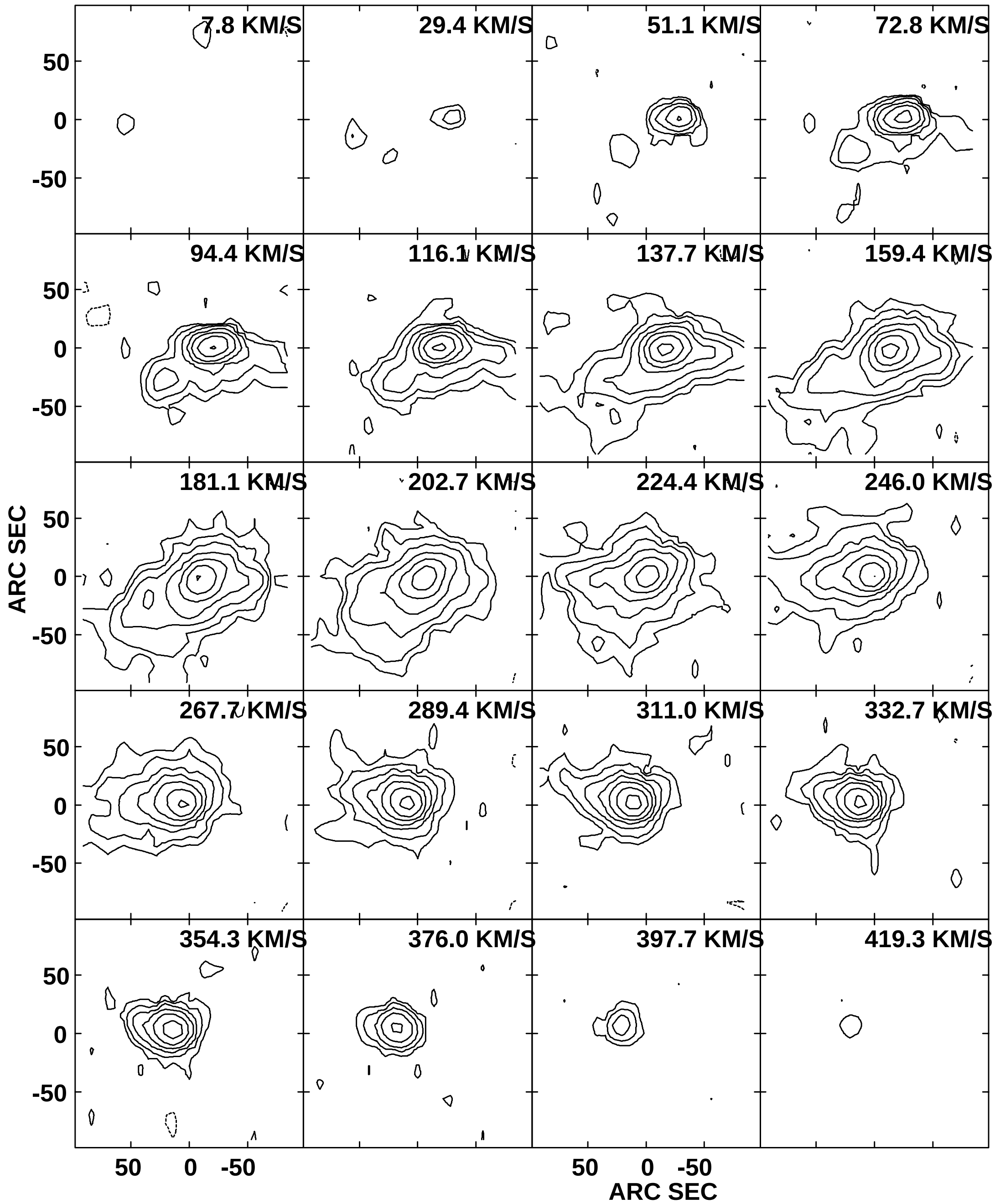

FIG. 1.—Channel maps of the distribution of ^{12}CO $J = 3$–2. The data cube has been Hanning smoothed to a resolution of 21.6 km s^{-1}, and the contour levels are 0.07 × (−1, 1, 2, 4, 8, 16, 32, 64) K. The major axis (*horizontal*) in this figure and all subsequent figures are at P.A. = 75°, and the offsets are relative to the 2 μm peak at $\alpha(2000) = 09^{\mathrm{h}}55^{\mathrm{m}}52\overset{\mathrm{s}}{.}3$, $\delta(2000) = 69°40'46''$. The spatial resolution for this and subsequent maps is 16″.

and CO $J = 2$–1 (Sofue et al. 1992; Thuma et al. 2000) and are also evident to a lesser degree in millimeter/submillimeter continuum (see, e.g., Krügel et al. 1990; Hughes, Gear, & Robson 1994; Kuno & Matsuo 1997; Alton et al. 1999; Thuma et al. 2000). The southeast feature appears more prominent in CO $J = 3$–2 than at lower transitions or in the continuum, indicating that this region of the outflow may be more highly excited than other regions.

The kinematic features of the outflow are generally evident in Figures 1, 2, and 4. These figures indicate the presence of rotation of the outflowing gas, in a sense consistent with that in the disk itself, persisting to heights of several hundred parsecs above and below the major axis. The effect presumably reflects the conservation of angular momentum in the outflowing gas. This rotation was noted in CO $J = 2$–1 by Loiseau et al. (1990) and Sofue et al. (1992), who also noted that the rotation in the halo is slower than in the disk. The effect is seen clearly in Figure 5, showing a series of "rotation curves" plotted versus height z above the disk in steps of 14″ (the telescope beamwidth). The velocities plotted in these curves were derived from Figure 4, and hence represent mean velocities. The plot shows a general flattening of the rotation curves with z and that the effect is more prominent south of the disk. Also evident from Figures 1, 2, 4, and 5 is a general redshift of the halo gas in the northern region and blueshift in the

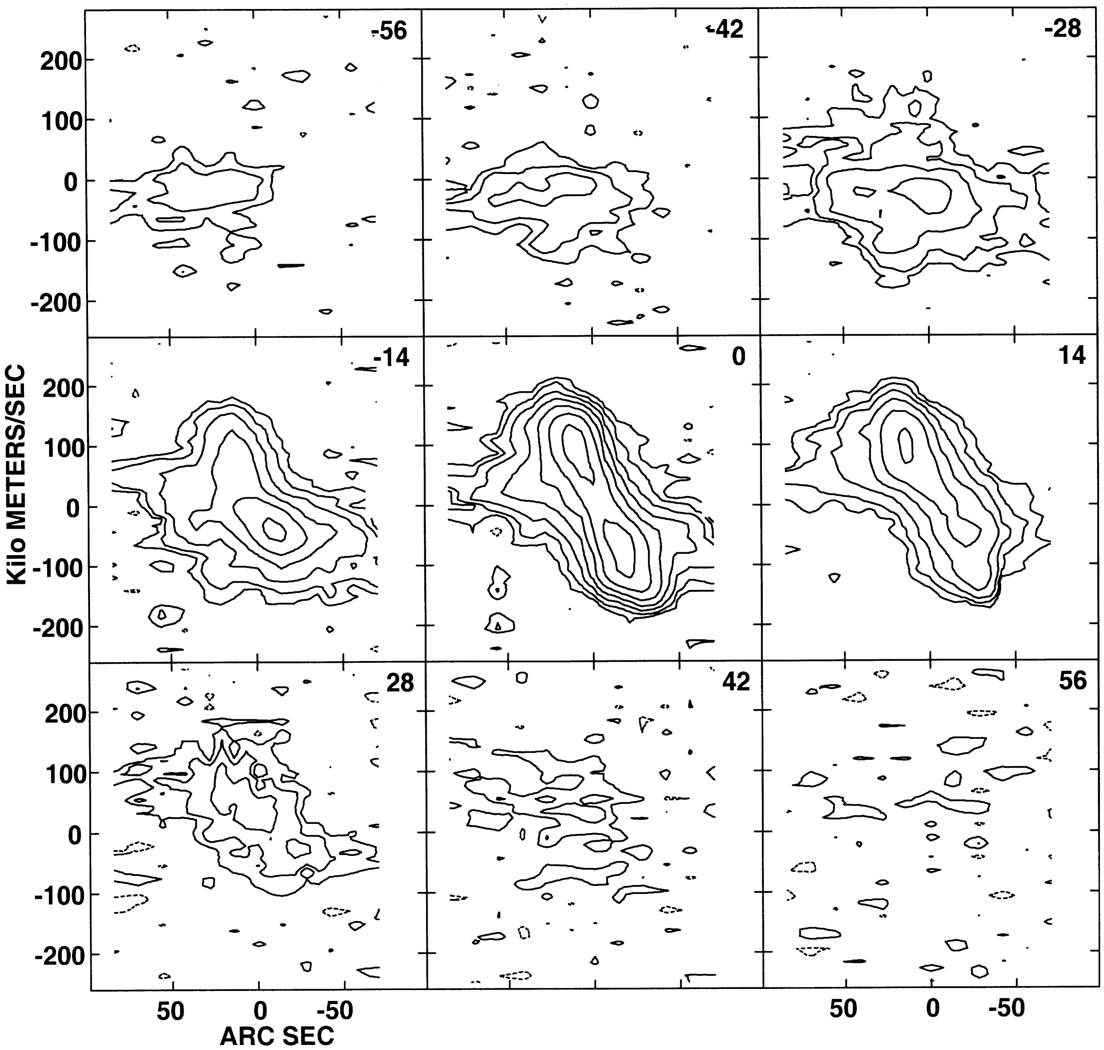

FIG. 2.—Position-velocity plots at various offsets above and below the major axis (specified in arcseconds). Contour levels are 0.07 × (−1, 1, 2, 4, 8, 16, 32, 64) K. Note that 1″ corresponds to a projected distance of 15.7 pc.

southern. In Figure 4 this effect is represented by a tilt of the isovelocity contours near the nucleus. This difference is qualitatively consistent with previous optical studies (e.g., Götz et al. 1990) and with an inclination of the disk (80°) with the northern part tipped away from the observer. The velocity shifts in the halo are more clearly represented in Figure 6, which is a plot of the mean velocity versus position along the minor axis. The gradient appears almost linear, with a slope of 58 km s^{-1} kpc^{-1}. There is no evidence of the splitting of the lines into two velocity regimes seen in the optical, attributable to the location of the gas on the surface of a cone. Also, the velocities of the molecular gas are generally lower than those seen in the optical (see, e.g., Fig. 2 of McKeith et al. 1995).

Also evident in these figures is the motion associated with the southeast spurlike feature. In the channel maps (Fig. 1) the spur appears as a very prominent extended feature to the southeast in the velocity range 50 km s^{-1} < V_{LSR} < 200 km s^{-1}. It also shows up in the p-v plots (Fig. 2) and the first-moment map in Figure 4, where it appears as a kink in the isovelocity contours in the southeast. The feature is significantly blueshifted relative to the local rotation of the galaxy (which is away from the observer) and even with respect to the systemic velocity. Its blueshift (up to −160 km s^{-1} relative to the systemic velocity) suggests that it is a part of the outflow that is the most strongly directed toward the observer (see § 5.2).

3.3. *Comparison among* ^{12}CO J = 3–2, ^{13}CO J = 3–2, $C^{18}O$ J = 3–2, *and* ^{12}CO J = 2–1

The emission observed in the two isotopes ^{13}CO and $C^{18}O$ was mapped over a smaller region of the disk and halo. To allow for global pointing uncertainties, comparisons between ^{13}CO and ^{12}CO J = 3–2 were made by aligning the integrated intensity maps, ensuring that the peak contours in the different maps are concentric, i.e., that the peak intensities are coincident. The assumption concerning the coincidence of peaks on the two maps is reasonable, given a similar agreement between ^{13}CO J = 1–0 and ^{12}CO J = 1–0 at higher angular resolution with the IRAM interferometer (Neininger et al. 1998). The ^{13}CO integrated brightness distribution in Figure 7 (*top panel*) shows a sharper gradient toward the south than the north, contrary to that seen in ^{12}CO. The map of the ratio ^{13}CO/^{12}CO in Figure 7 (*bottom panel*) shows a decrease in the ratio in all directions away from the nuclear disk, with a possibly stronger gradient toward the south. However, some caution should be exercised in accepting the magnitude of the gra-

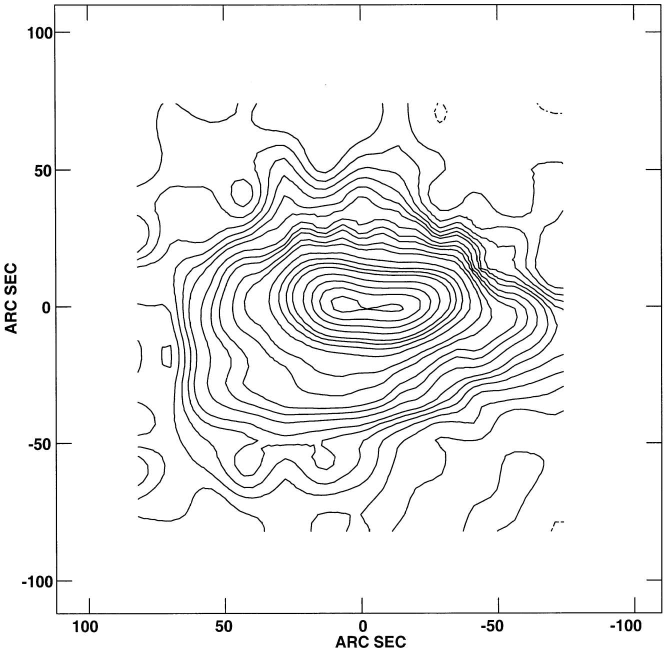

FIG. 3.—Map of the integrated intensity over the velocity range V_{LSR} = 0–450 km s^{-1}. Contour levels are 5.0 × (−1, 1, 2, 3, 4, 5, 6, 8, 10, 12, 16, 20, 30, 40, 50, 60, 80, 100, 120, 140) K km s^{-1}.

dient since the result is sensitive to random pointing errors, regardless of the alignment procedure outlined above. The primary result, which is the systematically lower ^{13}CO/^{12}CO ratio outside the starburst disk, is not attributable to the effects of pointing errors. The peak ratio is 0.11 in the part of the molecular ring (or bar) on the east side of the nuclear disk, falling to 0.05 at 150 pc below the disk, 220 pc above the disk, and 450 pc east and west of the nucleus.

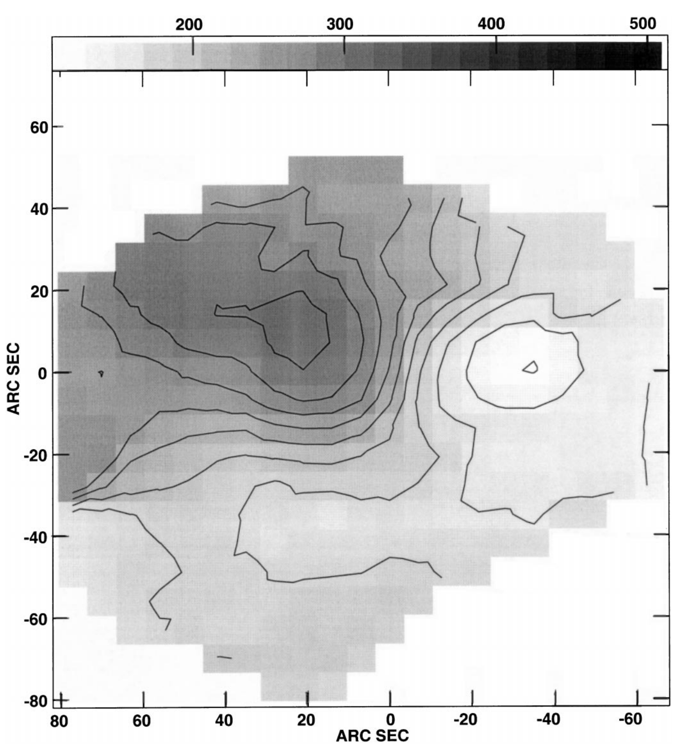

FIG. 4.—Map of the intensity-weighted mean velocity (first moment). Contours are 20 × (6, 7, 8, 9, 10, 11, 12, 13, 14, 15) km s^{-1}.

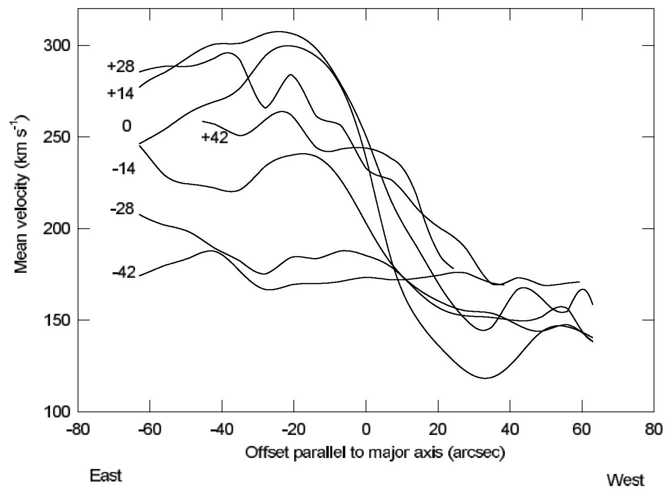

FIG. 5.—Plots of mean velocity from first-moment map (Fig. 4) vs. distance parallel to the major axis (rotation curves) for different offsets (arcseconds) from the major axis. The curve with the steepest slope in the central region corresponds to an offset equal to 0″.

A comparison was also made between our CO $J = 3$–2 map and a CO $J = 2$–1 map made with the IRAM 30 m antenna published by Thuma et al. (1999) and provided to us by N. Neininger. These data were convolved to the resolution of our CO $J = 3$–2 map. Figure 9 shows the ratio $J = 3$–$2/J = 2$–1 for the integrated intensities, representing a measure of the relative excitation of the two transitions. The prevailing trend in this map, as in the case of the ^{13}CO/^{12}CO ratio, is a decrease in the ratio in the halo and outer regions of the disk relative to the central disk. The peak ratio measured in the nuclear disk is about 0.8, and the ratio at 20″–30″ away from the nucleus is 0.4–0.5. There is evidence for regions where the ratio is higher in several regions away from the central disk, but caution needs to be exercised in the interpretation of these features at a detailed level since, as noted earlier, maps at both transitions are subject to the effects of random pointing errors. However, the region of higher ratio at 30″ southeast is consistent with the strength of the southeast spur in the ^{12}CO $J = 3$–2 transition. These results, together with the significance in the variation in the isotope ratio, are discussed in § 4.2.

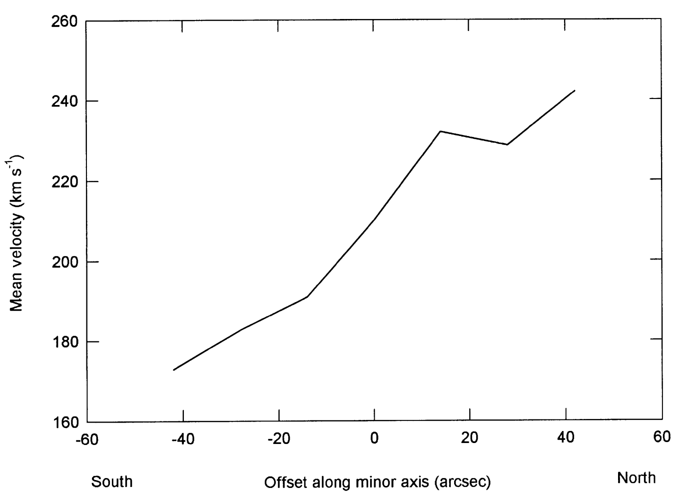

FIG. 6.—Mean velocity vs. distance (arcseconds) measured along the minor axis.

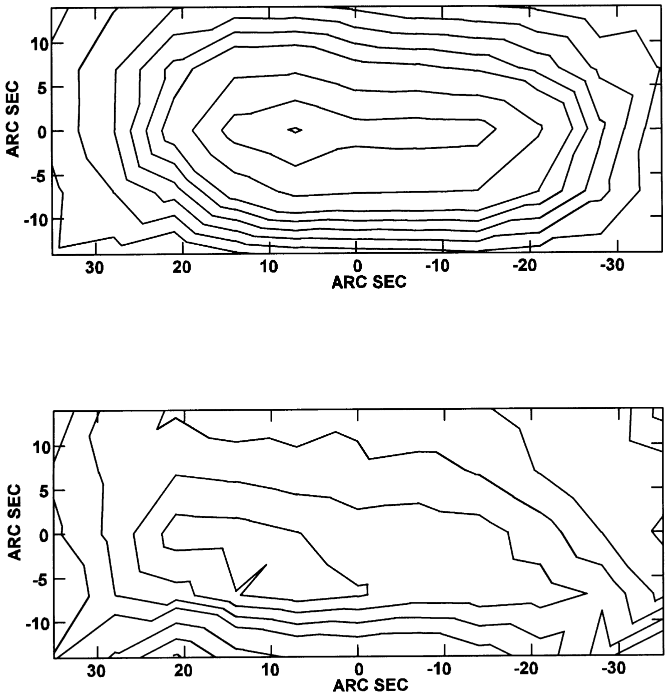

FIG. 7.—*Top*: Map of ^{13}CO $J = 3$–2 integrated intensity ratio (0–450 km s^{-1}) for the region surrounding the star-forming disk. Contour intervals are 5.0 × (1, 2, 3, 4, 5, 6, 8, 10, 12) K km s^{-1}. *Bottom*: Map of the integrated intensity ratio ^{13}CO/^{12}CO $J = 3$–2 for the region surrounding the star-forming disk. Contours are 0.1 × (1, 3, 5, 6, 7, 8).

The profiles of the four transitions, including the two isotopes in Figure 8, also show relevant line ratios over regions where the line strength is sufficient. The CO $J = 2$–1 cube was convolved from 11″ to the same resolution as our data for the purpose of this comparison. Note that the resolution in this case is 14″, as determined by the five C^{18}O profiles, and not 16″, as for all maps. Although the line ratio profiles cover a limited spatial region, they provide information beyond the starburst disk itself because of sampling the line of sight over a broad velocity range. The channel intensity ratios for ^{13}CO/^{12}CO, C^{18}O/^{12}CO, and CO $J = 3$–2/2–1 associated with the profiles are generally highest at the terminal or rotation velocities associated with the starburst disk. Accordingly, these profiles independently confirm the spatial variations in the ^{13}CO/^{12}CO and CO $J = 3$–2/2–1 integrated intensity ratios noted above, which show a peak in the region of the molecular ring. An interesting exception occurs in the CO $J = 3$–2/2–1 ratio 7″ east at "forbidden" velocities blueshifted relative to the systemic velocity, i.e., opposed to the sense of rotation. This anomalous feature of the ratio profile appears to confirm the enhancement in excitation seen in the "spur region" since this is the velocity region occupied by this feature. The indication is that this feature then corresponds to the portion of this spur that emerges from the disk near the east side of the molecular torus.

4. PHYSICAL CONDITIONS IN THE HALO GAS

4.1. *High- and Low-Excitation Components in the Disk*

It is beyond the scope of this paper to discuss the physical conditions in the disk in detail, since recent papers (e.g., Güsten et al. 1993; Mao et al. 2000; Weiss et al. 2001) develop detailed models based on more transitions and/or higher spatial resolution. However, these conditions are relevant for comparison with halo conditions, and consequently we discuss this region briefly. The studies referred to identify both a high-excitation (HE) and a low-excitation

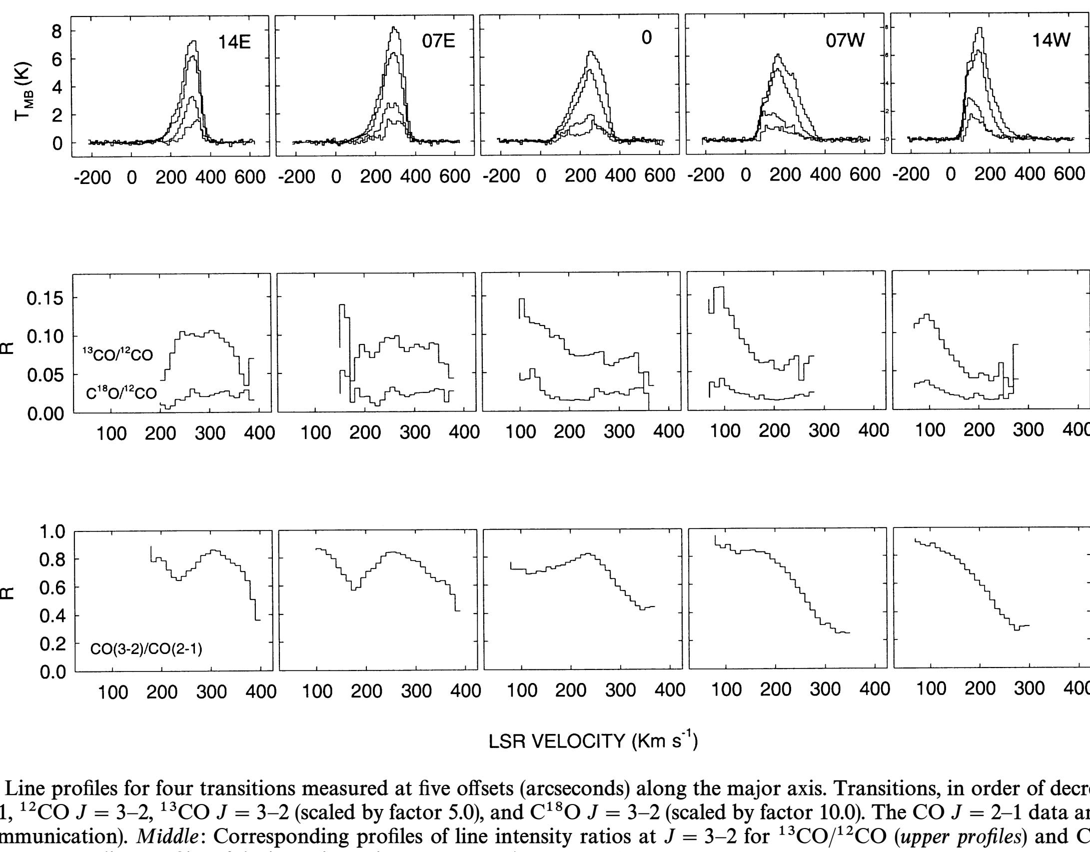

FIG. 8.—*Top*: Line profiles for four transitions measured at five offsets (arcseconds) along the major axis. Transitions, in order of decreasing amplitude, are ^{12}CO $J = 2$–1, ^{12}CO $J = 3$–2, ^{13}CO $J = 3$–2 (scaled by factor 5.0), and C^{18}O $J = 3$–2 (scaled by factor 10.0). The CO $J = 2$–1 data are from Neininger (2000, private communication). *Middle*: Corresponding profiles of line intensity ratios at $J = 3$–2 for ^{13}CO/^{12}CO (*upper profiles*) and C^{18}O/^{12}CO (*lower profiles*). *Bottom*: Corresponding profiles of the intensity ratio CO $J = 3$–2/CO $J = 2$–1.

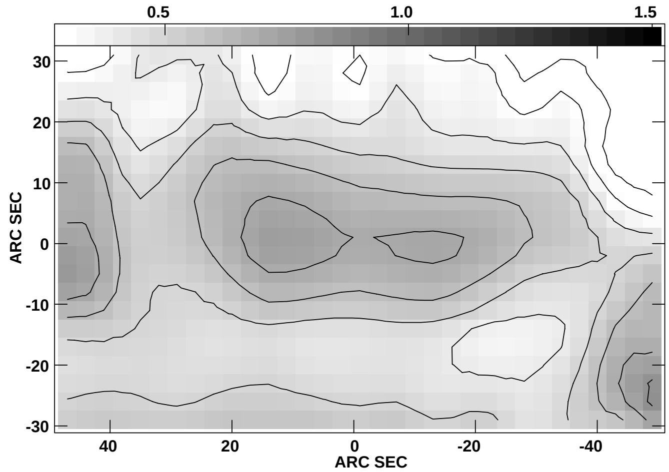

FIG. 9.—Map of the ratio of integrated intensities (over 0–450 km s^{-1}) for ^{12}CO $J = 3$–$2/J = 2$–1 using CO $J = 2$–1 data provided by N. Neininger (2000, private communication). Contours are $0.1 \times (3, 4, 5, 6, 7, 8)$.

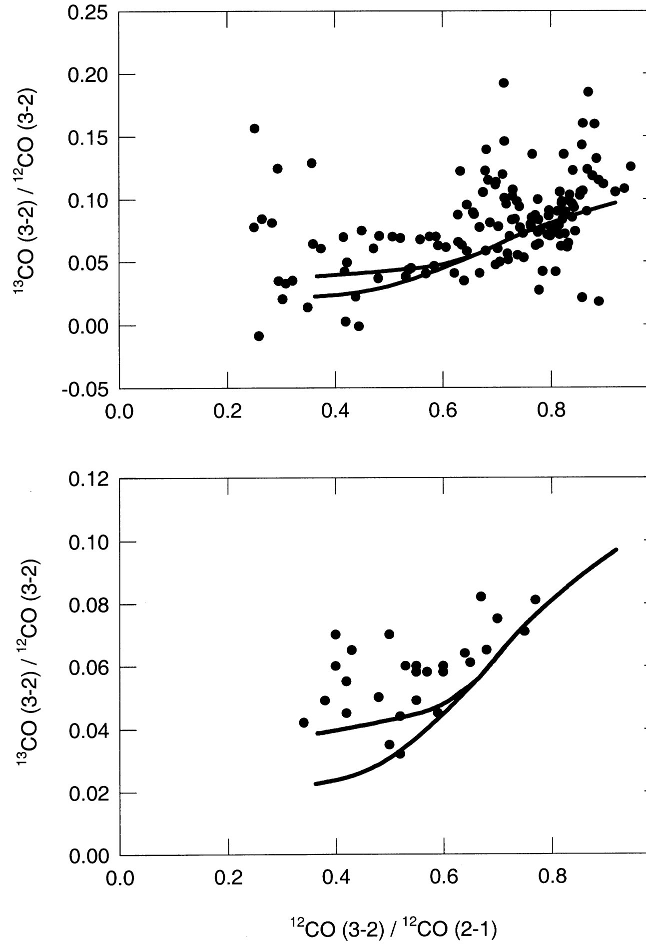

FIG. 10.—*Top*: Plot of ^{13}CO/^{12}CO $J = 3$–2 vs. ^{12}CO $J = 3$–$2/^{12}$CO $J = 2$–1 based on the line profile ratios in Fig. 8. The curve represents the expected behavior for a transition from a two-component model in the star-forming disk to the low-excitation (25 K) component in the outer regions, together with a decline in kinetic temperature from 25 to 10 K at 10^3 cm^{-3} (*upper fork*), or a decline in density from 10^3 to 10^2 cm^{-3} at 25 K (*lower fork*). See text for details. *Bottom*: Similar plot utilizing ratios of integrated line intensities obtained from Figs. 7 and 9. The poor fit of the curve is due to the use of integrated line intensities, whereas the model is based on peak line intensities. See text for details.

(LE) component. However, the parameters derived for these components are not well constrained by the observations and modeling procedures to date, since they vary considerably among the authors according to the method of analysis (e.g., large velocity gradient [LVG] vs. photodissocitaion region [PDR] models) and resolution employed. For the sake of definiteness, we adopt model 2*a* of Güsten et al. (1993), comprising an HE component with $T = 70$ K and $n = 10^5$ cm^{-3} and an LE component with $T = 25$ K and $n = 10^3$ cm^{-3}, since this work best matches our frequency coverage, spatial resolution, and modeling methods. Using LVG methods, we find good agreement between this model and our peak line brightness temperatures (as well as their line ratios) in the inner 500 pc of the disk, provided we adopt dilution factors $F = 0.075$ and 0.150 for the HE and LE components, respectively, a CO column density of 1.2×10^{17} cm^{-2} (km $s^{-1})^{-1}$ for the average cloud in each component, and an abundance ratio of $[^{12}CO/^{13}CO] = 40$. The dilution factor F represents the ratio of the observed to model brightness temperatures and is equivalent to the product of the area and velocity filling factors (see, e.g., Martin, Sanders, & Hills 1984; Richardson et al. 1986).

With an assumed abundance of $[^{12}CO/H_2] = 10^{-4.5}$, this model yields a column density for H_2 in the disk of 1.1×10^{23} cm^{-2}. For comparison, we used our $C^{18}O$ measurement and equation (3) of Wild et al. (1992) to obtain $N(H_2) = 5.5 \times 10^{22}$ cm^{-2}. This equation was modified to reflect our abundance ratio $[^{12}CO/C^{18}O] = 170$ derived from our LVG analysis. The corresponding mass of H_2 in the starburst disk, with an assumed size of $36'' \times 9''$ (560×140 pc; Hughes et al. 1994) is $(0.7$–$1.4) \times 10^8$ $M_\odot$.

4.2. *Physical Conditions in the Halo and Outer Disk*

Figures 7, 8, and 9 show that both the ^{13}CO/^{12}CO isotope intensity ratio and the CO $J = 3$–$2/J = 2$–1 excitation ratio have their highest values in the starburst disk. The same is probably true of the $C^{18}O/^{12}CO$ intensity ratio based on Figure 8. Figure 10 confirms the positive correlation between the ^{13}CO/^{12}CO and CO $J = 3$–$2/J = 2$–1 ratios. The upper panel is based on channel intensity ratios in Figure 8, and the bottom panel is based on the integrated intensity ratios in Figures 7 and 9. These variations are possibly attributable to the effects of a transition in excitation and cloud optical depth between the starburst and outer regions. We develop a simple illustrative model for this variation based on an extension of the cloud model for the disk discussed in § 4.1. Our LVG model representing the inner disk (combining both components) yields brightness temperature ratios for $J = 3$–$2/J = 2$–1 and ^{13}CO/^{12}CO of 0.92 and 0.077, respectively. However, the LE component alone has corresponding ratios of 0.66 and 0.045, respectively. Both components share the same ^{13}CO/^{12}CO abundance ratio, so that excitation and optical depth alone are responsible for these differences. The curves through the data in Figure 10 show the expected variation in the line ratios when the filling factor for the HE component is reduced, through a series of intermediate values, to zero, which occurs at the fork in the curve. The forked portion of the curve illustrates the behavior obtained from an LVG analysis by reducing the excitation of the LE component, which is assumed to be the only one remaining outside the starburst disk. The upper branch of the fork corresponds to a decrease in kinetic temperature from 25 to 10 K at $n = 10^3$ cm^{-3} and the lower branch to a decrease in density from 10^3 to 10^2 cm^{-3} at $T = 25$ K. In the latter case the associated column density N was assumed to decrease according to $N \propto n^{2/3}$, appropriate to an isotropic expansion of the clouds (e.g., in the outflowing wind). The model curve shows a better fit to the profile data (*upper panel*) since the model for the inner disk is based on peak line intensities, also represented in the data for the upper panel, and not integrated intensities, which are used in the lower panel. The latter represent average conditions along the line of sight. We emphasize that this example is illustrative only. Other models may well produce a similar result. However, our model demonstrates that the variations in isotope and excitation intensity ratios may be understood in terms of cooler and/or more rarefied clouds in the outer regions.

The observed variation in the line ratios is relevant to the more general observation of the ^{13}CO depression in luminous starburst galaxies relative to that in normal galaxies (see, e.g., Taniguchi, Ohyama, & Sanders 1999). The origin is not understood, but Taniguchi et al. suggest that the cause is related to the presence of a superwind in starburst galaxies. This hypothesis is supported by our results on M82, which further suggest that the excitation and isotope ratios should be correlated in starburst galaxies. Figure 5 of Taniguchi et al., based on the ratios ^{13}CO/^{12}CO $J = 1$–0 (R_{1-0}) and $J = 2$–$1/J = 1$–0, shows no correlation, but the substitution of R_{2-1} for R_{1-0} from their Table 1 does introduce a marginal correlation. Using the statistical software package ASURV Revsion 1.3 (see Isobe, Feigelson, & Nelson 1986 and references therein), we find a slope coefficient of 0.065 ± 0.018. Thus isotope ratios at higher excitation may provide a better test of the suspected correlation.

4.3. *Contribution of* CO $J = 3$–2 *to* 850 μm *Continuum*

We have compared our CO $J = 3$–2 map with the 850 μm observations of M82 made by Alton et al. (1999) using the Submillimeter Common-User Bolometer Array (SCUBA) on the JCMT. The purpose was to determine what fraction of the brightness in the continuum map is attributable to the integrated emission by CO, since the latter falls near the center of the SCUBA band. Using a SCUBA bandwidth of 30 GHz, appropriate to the epoch of the 850 μm observations, we estimate that the effective contribution to the continuum brightness for a beam size of 15."7 is given by

$$I = 9.2 \times 10^{-4} \int T_{\rm mb}\, dv \text{ Jy beam}^{-1} . \qquad (1)$$

Figure 11 shows the ratio of the CO contribution to the SCUBA filter to the continuum map of Figure 1*b* of Alton et al. (1999), which was convolved to the resolution (16") of our CO map. This ratio represents the fractional contribution of CO to the continuum. The ratio map displays a curious "quadrupole" appearance, signifying strong contributions (70%) from the outer disk at ±30" (±470 pc), modest contributions (~40%) from the molecular ring or bar, and relatively weak contributions (20%) in the halo. The areas of strongest contribution by CO are thus the regions of the spurs at the edge of the outflow in the disk. These two regions, in turn, are interior to two "warm spots" in the excitation map of Figure 9. The conclusion is that a significant fraction of the SCUBA 850 μm continuum is produced by CO $J = 3$–2 emission, especially in the disk and regions where the outflow originates in the starburst disk. The total contribution by CO to the integrated

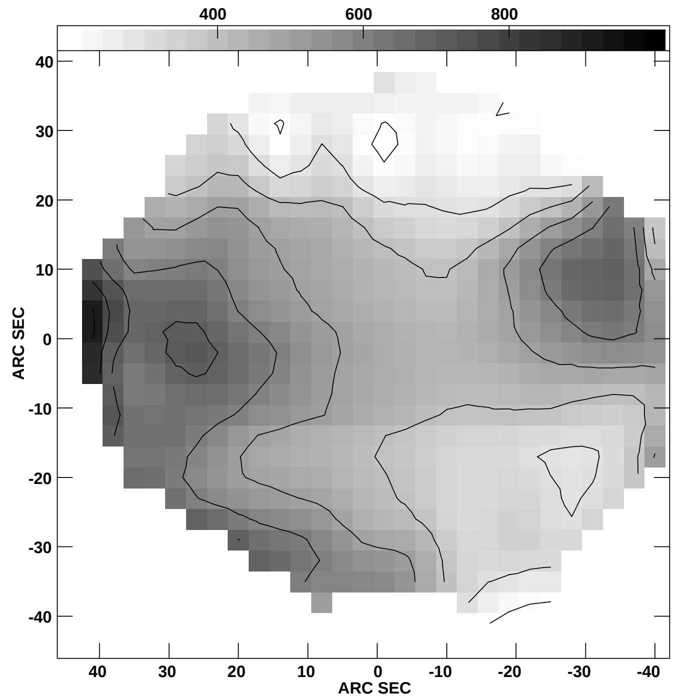

FIG. 11.—Map of the ratio of the contribution of the ^{12}CO $J = 3$–2 brightness to the SCUBA band vs. the 850 μm brightness based on the continuum map of Alton et al. (1999). The latter was convolved to 16" resolution to match our CO map in Fig. 3. Contour levels are 0.1 × (−1, 1, 2, 3, 4, 5, 6, 7).

SCUBA flux is 47%. This contribution is relatively higher than that by the CO $J = 2$–1 line to the 1.3 mm continuum found by Thuma et al. (2000). This is largely because of the relatively wider (by 50%) Doppler frequency width of the CO $J = 3$–2 transition and the narrower bandwidth of SCUBA relative to that of the MPIR 1.3 mm imaging bolometer used by Thuma et al. (2000). This result suggests that the factor $X_{\rm CO}$ for converting CO $J = 1$–0 intensities to H_2 column density might be strongly variable over the disk and halo region of M82 and that the two observables do not both trace the molecular gas content alone. Note that Weiss et al. (2001) also infer a variation in this parameter across the starburst disk.

5. THE NATURE OF THE HALO GAS

5.1. *Kinematics*

The p-v plots in Figure 2 show good agreement with similar plots at lower transitions (e.g., CO $J = 2$–1 by Sofue et al. 1992). Emission can be traced out to about ±185 km s^{-1} with respect to the systemic velocity. The rotation curve in the disk exhibits a constant slope of 6.8 km s^{-1} arcsec^{-1} within ±12" (190 pc) of the nucleus. Within the errors of measurement, the spacing between the two lobes is identical to that in seen in the map by Sofue et al. (1992) both in velocity and in distance. Beyond 190 pc, the velocity decreases, perhaps in a Keplerian fashion as suggested by Sofue et al. There is insufficient spatial resolution to discern the "figure eight" pattern attributed by Neininger et al. (1998) to orbits under the influence of the central bar, nor is it possible to study peculiar features such as the "superbubble" (Weiss et al. 1999; Wills et al. 1999).

As noted in § 3.2, several previous studies have pointed to rotation of the halo gas, reflected in p-v plots measured parallel to the major axis above and below the disk. Figures 2, 5, and 6 confirm these earlier studies showing that the "rotation curves" offset from the major axis are both shallower and exhibit a different systemic velocity relative to that in the disk. Figures 5 and 6 were made using the first-moment map (Fig. 4) and therefore reflect intensity-weighted mean velocities. The plot of mean velocity measured on the minor axis shows radial velocities of +32 and -37 km s^{-1} at 40″ above and below the disk, respectively. These motions are in agreement with previous studies at CO $J = 1$–0 and $J = 2$–1 (e.g., Nakai et al. 1987; Loiseau et al. 1990; Sofue et al. 1992) and correspond to the combined effects of the inclination of the disk $i = 80°$ and the outflow from the starburst region. The inferred (deprojected) outflow speed is $\approx$200 km s^{-1} at 600 pc above and below the disk. This figure compares with 600 km s^{-1} suggested by the optical data (McKeith et al. 1995; Shopbell & Bland-Hawthorn 1998).

The flattening of the rotation curves above and below the disk has been attributed to the conservation of angular momentum in the outflowing gas (see, e.g., Sofue et al. 1992). The flattening is thus associated with a divergence of the flow as the gas expands outward. We take this hypothesis one step further and assume that conservation of angular momentum implies that the quantity $L(r, z) = rV(r, z)$ is conserved along a given trajectory in the flow, where $V(r, z)$ is the terminal velocity at distance r from the minor axis and height z above the major axis. Such a "flow trajectory" thus connects in principle the terminal velocity point at one value of z to that at another along the outflow. The mean velocities from Figure 6 were used to represent $V(r, z)$. Though the values derived in this way do not represent strictly the true terminal velocity, they are obtainable in an objective way from the data cube. Points defined by $L(r, z)$ = constant at various values of z in Figure 6 were then used to generate a series of such flow lines, as shown in Figure 12. Note that if $V(r, z)$ represents material in a rotating ring instead of the terminal velocity within a differentially rotating disk, then the analysis is still valid, but the trajectories would in this case be projections of the flow lines onto the plane of the sky. Although individual flow lines in Figure 12 should not be taken too seriously, the collective result is significant in indicating the mean divergence of the flow. For example, it shows that the divergence is significantly greater below the plane than above, which is consistent with the more strongly blueshifted motions in the southeast. The average cone angles are about 40° in the north and 90° in the south, with an overall average of about 65°. Recent estimates of this cone angle based on modeling the optical data, using different methods from that described here, produce cone angles ranging from 30°–35° (Bland & Tully 1988; Götz et al. 1990; McKeith et al. 1995) to 60°–65° (Heckman, Armus, & Miley 1990). The larger cone angle below the plane and lower velocities for the molecular gas suggest significantly different dynamical behavior between ionized and cold molecular gas. It is useful to note that as the outflow carries a given layer of material outward from the disk, the tangential motions of the gas originally associated with rotation in the disk are transformed asymptotically into a component directed radially outward and parallel to the disk as expansion proceeds. If this radial component has magnitude V_t and the wind speed is V_w along the minor axis, then the resultant cone angle resulting from free expansion is $2\tan^{-1} (V_t/V_w)$. With $V_t \sim 100$ km s^{-1} at the edge of the molecular ring and $V_w \sim 200$ km s^{-1}, the cone angle expected is about 50°, which is consistent with that observed.

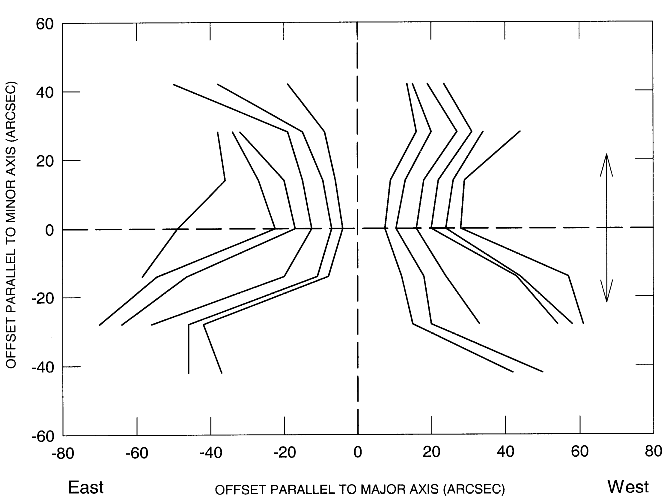

FIG. 12.—Plot of "flow lines" of molecular gas in the outflow region from an analysis based on the flattening of the rotation curves and the assumption that angular momentum is conserved in the outflow. The arrows to the right indicate the flow directions. See text for details.

5.2. *Mass and Energetics*

The mass of molecular hydrogen was estimated using both the CO and 850 μm emission observed by Alton et al. (1999), after correcting their map for the contribution by CO $J = 3$–2 emission. In both cases, the halo flux was estimated by blanking out the disk, based on a region 36″ × 9″ (560 × 140 pc), following the method of Alton et al. (1999). The halo CO flux was converted to an H_2 mass using the LE component model with the upper branch of the curve in Figure 10 ($n = 10^3$ cm^{-3} and variable temperature). The lower branch ($T = 25$ K and variable density) was found to produce very low model brightness temperatures requiring dilution factors greater than unity. The derived molecular gas mass for the range 13 K $\leq T \leq$ 25 K is 4.4×10^8 $M_\odot \leq M_g \leq 1.2 \times 10^9$ $M_\odot$, with the higher mass associated with the lower temperature. The mass was also derived using a standard factor for the Galaxy, namely $X_{CO} = 1.6 \times 10^{20}$ cm^{-2} (K km s^{-1})$^{-1}$ derived by Hunter et al. (1997), with the result $M_g = 1.1 \times 10^9$ $M_\odot$. Note that our CO fluxes for the halo are likely to be overestimated by up to 30%, allowing for the effects of the error beam. Also, applying the standard galactic value of X_{CO} is likely to overestimate the flux, since the value for this parameter may be lower in starburst galaxies (see, e.g., Wild et al. 1992; Weiss et al. 2001). The mass based on the 850 μm emission was derived by scaling the values derived by Alton et al. (1999) by the ratio of the CO-corrected to uncorrected halo flux densities. With their assumed dust temperatures in the range 13 K $\leq T_d \leq$ 30 K and dust emissivity index $1 \leq \beta \leq 2$, and assuming a gas-to-dust ratio of 100, the result is 1.0×10^8 $M_\odot \leq M_g \leq 6.0 \times 10^8$ $M_\odot$, or about a factor of 2 lower than those inferred from Alton et al. Taking all factors into account, we adopt a value of 5×10^8 $M_\odot$ as a reasonable estimate for the mass of H_2 in the halo, with an uncertainty of about a factor of 2. Recall that our estimate for the molecular gas in the disk (§ 4.1) was $\sim 10^8$ $M_\odot$, indicating that there may be more cool gas in the halo than in the starburst disk itself! The mass adopted for the halo is also in accord with estimates for the total mass of H_2 in M82 by Thuma et al. (2000), although this value includes the gas in the disk. For comparison, we estimate that the minimum mass of H I within a comparable region from Figure 2 of Yun, Ho, & Lo (1993) is 2×10^7 $M_\odot$, also predominantly outflowing but with some evidence for infall. The H_2 mass of 5×10^8 $M_\odot$ exceeds the estimate by Nakai et al. (1987), based on CO $J = 1$–0, by an order of magnitude. We attribute this difference largely to their assumption that the CO $J = 1$–0 transition in the halo is optically thin. This assumption was motivated by the result, prevalent at the time, that the CO $J = 2$–1/CO $J = 1$–0 ratio was significantly greater than unity. Observations since that time have not borne out this result, and such line ratios, at least for the disk, can now be firmly rejected (Weiss et al. 2001). Comparison between the CO $J = 1$–0 measurements of Nakai et al. (1987) and the map provided by N. Neininger, convolved to the same resolution, also show no significant evidence for such ratios. However, since this ratio also depends on the excitation temperature, a key measurement relating to this point would be the ^{13}CO/^{12}CO $J = 1$–0 intensity ratio in the halo.

If we take a mean expansion velocity of 100 km s^{-1}, then the kinetic energy and momentum associated with the molecular gas outflow are 5×10^{55} ergs and 1×10^{49} g cm s^{-1}, respectively. If we furthermore consider a representative size of 1 kpc, we infer an expansion timescale of about 10^7 yr, which is significantly shorter than the age of the starburst (about 5×10^7 yr according to O'Connell et al. 1995). The associated rate of mass injection is then 50 $M_\odot$ yr^{-1}, and the required energy and momentum injection rates are 5.0×10^{48} ergs yr^{-1} and 1×10^{42} g cm s^{-1} yr^{-1}, respectively. These figures may be compared with available supply. Adopting a supernova rate of 0.1 yr^{-1} with 10^{51} ergs per supernova, we obtain a total energy input of $\dot{E} = 10^{50}$ ergs yr^{-1} and a mass injection rate of $\dot{M} = 1$ $M_\odot$ yr^{-1} (Suchkov et al. 1996). Then, without further mass loading, a wind speed $V[= (2\dot{E}/\dot{M})^{1/2}] = 3000$ km s^{-1} is inferred, which leads to a momentum injection rate of $\dot{P} = 6 \times 10^{41}$ g cm s^{-1} yr $^{-1}$. Thus the figures for the energy and momentum of the molecular gas inferred from our CO data are within the allowable range, if essentially all momentum available is transferred to the molecular gas. However, the inferred mass-loading rate exceeds current estimates from models by about an order of magnitude (see, e.g., Suchkov et al. 1996), and it is also unlikely that a mass loss rate of 50 $M_\odot$ yr^{-1} could be sustained over the life of the starburst, which would require a total supply of 2.5×10^9 $M_\odot$.

The high mass-loading rate, together with the observation that most of the molecular gas in M82 may be located in the halo, suggests that the observed gas may not escape from the galaxy and may instead fall back to the disk. It may be recycled as a "fountain" through the halo, possibly the consequence of multiple superbubbles or supershells resulting from starburst events. The superbubble with mass 8×10^6 $M_\odot$ reported by Weiss et al. (1999) may represent one such event. This interpretation would be in accord with the rough proportionality between velocity and displacement, since low-velocity gas would attain a lower maximum height above the disk. In addition, the mass of the molecular gas in the halo is in accord with supershells observed in other galaxies (see, e.g., Rand & Stone 1996; Lee & Irwin 1997; Lee 1998), which are of the order of 10^8 $M_\odot$. This general picture is supported by the observation that the maximum expansion velocity is comparable to the escape velocity (approximately 200 km s^{-1}), indicating that much of the gas would be bound to the galaxy if only gravitational forces are considered. There is also a suggestion from Figure 12 that the flow vectors show an increasing divergence with z, which supports this view, though other explanations for this effect may also be possible. To further assess the physical plausibility that much of the molecular gas is gravitationally bound to M82, we evaluate the ratio R of gravitational force to the maximum thrust associated with the momentum of the wind. If we adopt for simplicity that gas of mass M_g is concentrated at height z of a few hundred parsecs or more, then this ratio is given approximately by $R = (M_g V_{esc}^2/2z\dot{P})f^{-1}$, where V_{esc} is the escape velocity and f is the area covering factor of the molecular gas seen by the wind. If we take $M_g = 10^8$ $M_\odot$, $V_{esc} = 200$ km s^{-1}, $z = 500$ pc, and the momentum injection rate $\dot{P}$ derived above, then this ratio has a value of $1.3f^{-1}$. Since $f \leq 1$, this result confirms that the gravitational force may dominate over the thrust of the wind. On the other hand, a possible objection to the suggestion that the molecular gas falls back to the disk is the lack of indication for much infalling gas in the data, although Figure 2 does show that some material along the minor axis is infalling. A possible explanation is that infalling CO has been dissociated by interaction with the wind or lack of shielding from the intense UV from the starburst region. A test of this hypothesis would be to search for infalling gas in another state, such as C I in the 492 GHz fine structure transition for example.

6. CONCLUSIONS

A map of M82 in ^{12}CO $J = 3$–2 shows that emission at this transition is detectable over a region 2.8×2.8 kpc centered on the nucleus. The inferred mass of H_2 in the halo is about 5×10^8 $M_\odot$ with a kinematic timescale of about 10^7 yr. The emission outside the starburst region appears brighter below the plane than above, partly the effect of a prominent spur extending to the southeast. The comparison between various transitions indicates that the prevailing trend in the line ratios $J = 3$–2/$J = 2$–1, ^{13}CO/^{12}CO $J = 3$–2, and C^{18}O/^{12}CO is a decrease away from the starburst region. These effects may be understood in terms of decreases in the excitation and optical depth of the outer disk and halo, although a unique model for the variation must await observations of many more transitions in the halo. This result has implications for the observation that starburst galaxies have lower ^{13}CO/^{12}CO intensity ratios than normal galaxies. Specifically, in analogy with M82, the superwind region of starburst galaxies may possess lower excitation and optical depth, which will lead to lower values for the isotopic ratios. If this interpretation is correct, there should be a correlation of the isotopic ratios, especially at higher transitions, with the excitation ratio among starburst galaxies.

A comparison of the integrated intensities of ^{12}CO $J = 3$–2 with the 850 μm continuum distribution observed by Alton et al. (1999) shows that CO makes a substantial contribution (47% overall) toward the continuum emission and that this contribution is higher in the region of concentrated brightness at the edge of the molecular ring (or bar). The variations are possibly related to the effects of excitation in the CO gas with position. A correction for the CO contribution is thus essential for the interpretation of the continuum data. This result also heightens concern over the usefulness of the parameter X_{CO} used to convert CO $J = 1$–0 line intensities directly to molecular gas mass in starburst galaxies, except in the crudest sense. Our CO $J = 3$–2 observations confirm many kinematic features seen at lower transitions, including the rotational properties of the disk and a radial expansion of the outflow at speeds up to 200 km s^{-1}, which is slower than that for ionized gas (600 km s^{-1}). They also confirm that gas in the outflow is rotating more slowly than that of the disk, which is readily attributable to the conservation of angular momentum in a conical outflow. An analysis of our data based on the assumption of conservation of angular momentum in the outflowing gas reveals that the cone angle for gas below the disk appears to be greater than for gas above the disk, which may be also related to the prominent spur toward the southeast.

Our observations and interpretation suggest that the dynamics of the entrained molecular gas are very different from the optically observed ionized gas. The lower expansion velocities, the possible predominance of molecular mass in the halo over that in the disk, and the inference of a wind mass-loading rate higher than that for current models, suggests that the halo gas may not be escaping from M82. Instead, the gas may correspond to "fountains" comprising multiple superbubbles or supershells ejected by transient star formation events, which fall back to and replenish the disk with molecular gas. A search for infalling gas, possibly in forms not visible in CO, may prove worthwhile.

The authors wish to thank N. Neininger, University of Bonn, Germany, for providing data for CO $J = 2$–1, observed with the IRAM 30 m telescope, and Paul Alton, University of Wales, UK, for providing electronic versions of SCUBA maps of M82. The authors also wish to thank the staff of the JCMT for their assistance in making most of the observations and also an anonymous referee for suggestions that improved the manuscript. This research was supported by a grant to E. R. S. from the Natural Sciences and Engineering Research Council of Canada.

REFERENCES

Achtermann, J. M., & Lacy, J. H. 1995, ApJ, 439, 163
Alton, P. B., Davies, J. I., & Bianchi, S. 1999, A&A, 343, 51
Bland, J., & Tully, R. B. 1988, Nature, 334, 43
Bregman, J. N., Schulman, E., & Tomisaka, K. 1995, ApJ, 439, 155
Dietz, R. D., Smith, J., Hackwell, R. D., Gehrz, R. D., & Grasdalen, G. L. 1986, AJ, 91, 758
Götz, M., McKeith, C. D., Downes, D., & Greve, A. 1990, A&A, 240, 52
Güsten, R., Serabyn, E., Kasemann, C., Schnickel, A., Schneider, G., Schulz, A., & Young, K. 1993, ApJ, 402, 537
Heckman, T. M., Armus, L., & Miley, G. K. 1990, ApJS, 74, 833
Hughes, D. H., Gear, W. K., & Robson, E. I. 1994, MNRAS, 270, 641
Hunter, et al. 1997, ApJ, 481, 205
Isobe, T., Feigelson, E. D., & Nelson, P. I. 1986, ApJ, 306, 490
Krügel, E., Chini, R., Klein, U., Lemke, R., Wielebinski, R., & Zylka, R. 1990, A&A, 240, 232
Kuno, N., & Matsuo, H. 1997, PASJ, 49, 265
Lee, S.-W. 1998, Ph.D. thesis, Queen's Univ.
Lee, S.-W., & Irwin, J. A. 1997, ApJ, 490, 247
Loiseau, N., Nakai, N., Sofue, Y., Wielebinski, R., Reuter, H.-P., & Klein, U. 1990, A&A, 228, 331
Mao, R. Q., Henkel, C., Schulz, A., Zielinsky, M., Mauersberger, R., Störzer, H., Wilson, T. L., & Gensheimer, P. 2000, A&A, 358, 433
Martin, H. M., Hills, R. E., & Sanders, D. B. 1984, MNRAS, 208, 35
McKeith, C. D., Greve, A., Downes, D., & Prada, F. 1995, A&A, 293, 703
Nakai, N., Hayashi, M., Handa, T., Sofue, Y., & Hasegawa, T. 1987, PASJ, 39, 685
Neininger, N., Guélin, M., Klein, U., García-Burillo, S., & Wielibinski, R. 1998, A&A, 339, 737
O'Connell, R., Gallagher, J., Hunter, D., & Wesley, C. 1995, ApJ, 446, L1
Rand, R. J., & Stone, J. M. 1996, AJ, 111, 190
Richardson, K. J., White, G. J., Phillips, J. P., & Avery, L. W. 1986, MNRAS, 219, 167
Reuter, H.-P., Klein, U., Wielibinski, R., & Kronberg, P. P. 1994, A&A, 282, 724
Seaquist, E. R., & Odegard, N. 1991, ApJ, 369, 320
Shen, J., & Lo, K. Y. 1995, ApJ, 445, L99
Shopbell, P. L., & Bland-Hawthorn, J. 1998, ApJ, 493, 129
Sofue, Y., Reuter, H.-P., Krause, M., Wielebinski, R., & Nakai, N. 1992, ApJ, 395, 126
Suchkov, A. A., Berman, V. G., Heckman, T. M., & Balsara, D. S. 1996, ApJ, 463, 528
Tammann, G. A., & Sandage, A. R. 1968, ApJ, 151, 825
Taniguchi, Y., Youichi, O., & Sanders, D. B. 1999, ApJ, 522, 214
Thuma, G., Neininger, N., Klein, U., & Wielebinski, R. 2000, A&A, 358, 65
Watson, M.G., Stanger, V., & Griffiths, R. E. 1984, ApJ, 286, 144
Weiss, A., Neininger, N., Hüttemeister, S., & Klein, U. 2001, A&A, 365, 571
Weiss, A., Walter, F., Neininger, N., & Klein, U. 1999, A&A, 345, L23
Wild, W., Harris, A. I., Eckart, A., Genzel, R., Graf, U. U., Jackson, J. M., Russell, A. P. G., & Stutski, J. 1992, A&A, 265, 447
Wills, K. A., Redman, M. P., Muxlow, T. W. B., & Pedlar, A. 1999, MNRAS, 309, 395
Yun, M. S., Ho, P. T., & Lo, K. Y. 1993, ApJ, 411, L17